

Internal Defect Detection in Ferromagnetic Material Equipment Based on Low-Frequency Electromagnetic Technique in 20# Steel Plate

Weimin Lou, Changyu Shen, Zhouhong Zhu, Zexu Liu, Fengying Shentu, Weixin Xu, Tingting Lang^{ID}, Yang Zhang, Zhenguo Jing, and Wei Peng^{ID}

Abstract—A ferromagnetic material equipment internal defect detection system based on low-frequency (20–50 Hz) electromagnetic technique was proposed. Direct current magnetization was used to make the ferromagnetic material sample (20# steel for instance) be in a saturation magnetization state to decrease its permeability, which is beneficial for increasing the skin depth of the sample and strengthening the signal of the magnetic flux leakage. A low-frequency alternating current source was used to excite the spatial alternating electromagnetic field and a Hall sensor was used to collect the signal of the spatial magnetic field. Experimental results showed that the 6-mm buried depth internal defect with the sensitivity of 0.05 mm can be detected in the 12-mm thick 20# steel plate or pipeline, which is almost 1.5 times higher than that of the current similar sensors.

Index Terms—Low frequency, saturation magnetization, internal defect detection.

I. INTRODUCTION

SPECIAL pressure equipment, such as oil storage tank and gasholder, are widely used in agricultural production and national defense. The equipment is usually made up of the ferromagnetic carbon steel, and they usually work in the environment of strong acid, high temperature and high pressure. Naturally, some cracks or defects inevitably occur inside these equipment as time went by. Hence, detecting these defects in an early stage or detecting in real time is necessary for the safety of the society. Magnetic flux leakage testing technology (MFL) is a traditional nondestructive testing technology

for ferromagnetic material equipment defect detection [1]–[3]. It mainly consists of three parts: excitation of spatial electromagnetic field, collection of magnetic field signal and processing of magnetic field signal. There are several excitation sources included permanent magnet (PM), direct current (DC) and alternative current (AC) excitations. PM and DC are similar. AC has high inspection sensitivity but is limited by skin effect [4]. The common magneto sensors for magnetic field signal collection include Hall sensor, anisotropic magneto-resistance (AMR) sensor, giant magneto-resistance (GMR) sensor and tunnel magneto-resistance (TMR) sensor [5]. Hall sensor is at a low cost and is the most used one.

Some heuristic algorithms [6]–[10] are applied in defect reconstruction such as genetic algorithm, simulated annealing algorithm, particle swarm optimization, and so on. Both of them exhibit prominent searching and optimization capacity. But usually the excessive amount of compute time is needed for the defect reconstruction.

Based on the conventional MFL structure of the three parts, several nondestructive testing methods were carried out. Sun *et al.* [11] proposed a permanent magnetic perturbation (PMP) testing method. This method is free from pipe end effect, magnetic compression effect and skin effect. And it does well in the Omni-directional defect detection. But this method is suffered from the lower signal-to-noise ratio. Gao *et al.* [12] combined electromagnetic mechanism of Joule heating with MFL and realized the visual inspection. But it only focuses on the simple surface defect detection. Wincheski *et al.* [13] utilized spin-dependent tunneling (SDT) sensor to detect the relative deeply internal flaw and fatigue cracks. However, the complex and relative expensive setup limit its applications.

In this paper, we proposed a low frequency electromagnetic technique (LFET) method for the internal defect detection in ferromagnetic material. Both DC and AC excitation were used. A Hall sensor with a high sensitivity of 25mV/Gs was used to collect spatial magnetic field signal. The signal was then processed by amplifier, filter, and rectification. Compared to the traditional MFL, the maximum detectable buried depth of internal defect is 6mm, which is almost 1.5 times higher than that of the current similar methods [5], [12], [14].

Manuscript received May 15, 2018; accepted June 25, 2018. Date of publication June 27, 2018; date of current version July 24, 2018. This work was supported in part by the National Key R&D Program of China under Grant 2017YFF0209703, in part by the National Major Scientific Research Instrument Development Project of the Natural Science Foundation of China under Grant 61727816, in part by the Public Project of Zhejiang Province under Grant LGG18F050003, and in part by the Special Fund for Quality Inspection Research in the Public Interest of China under Grant 201510066. The associate editor coordinating the review of this paper and approving it for publication was Prof. Gijs J. M. Krijnen. (Corresponding author: Changyu Shen.)

W. Lou, C. Shen, Z. Zhu, Z. Liu, F. Shentu, W. Xu, and T. Lang are with the Institute of Optoelectronic Technology, China Jiliang University, Hangzhou 310018, China (e-mail: shenchangyu@cjljlu.edu.cn; s1504080306@stu.cjljlu.edu.cn).

Y. Zhang, Z. Jing, and W. Peng are with the School of Physics and Optoelectronic Technology, Dalian University of Technology, Dalian 116024, China.

Digital Object Identifier 10.1109/JSEN.2018.2850977

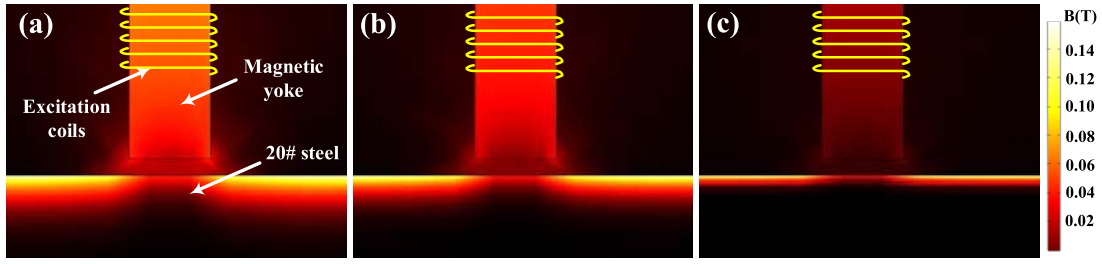


Fig. 1. Electromagnetic field energy distributions with different excitation frequency of (a) 50Hz, (b) 100Hz and (c) 1000Hz.

TABLE I
COMPARISON BETWEEN TWO THEORETICAL ANALYSES

	Magnetic dipole model	PDE model
Magnetic field source	Magnetic charge	Molecular current
Elementary parameter	\mathbf{H}	\mathbf{B}
Evaluation method	Magnetic Coulomb's law	Finite element analysis

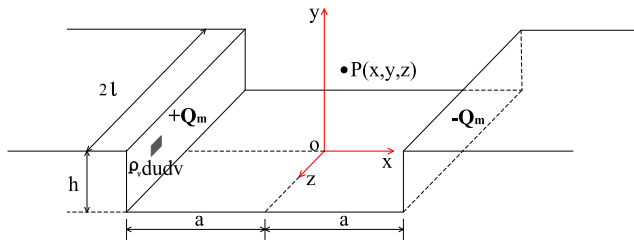


Fig. 2. Schematic of magnetic dipole model.

II. THEORETICAL ANALYSIS

When an alternating electromagnetic field is applied on the ferromagnetic material (20# steel for instance), the energy of electromagnetic field does not distribute evenly within the sample. The main energy is in the sample steel surface and attenuates gradually with the increase of the penetration distance due to the skin effect. Fig. 1 shows the simulated electromagnetic field energy distributions for different excitation frequency of (a) 50Hz, (b) 100Hz and (c) 1000Hz. It can be seen that the magnetic energy enters into the sample steel much deeper when the excitation frequency is lower at the same conditions of lift-off, the number of turns, excitation intensity and so on.

In order to obtain the exactly value of the perturbation of the spatial electromagnetic field, there are two models [15], [16] for the calculation of the exact electromagnetic intensity value in a region above defects. One is magnetic dipole model and the other is partial differential equations (PDE) model originated from Maxwell's equations, as illustrated in Table I.

A. Magnetic Dipole Model

In magnetic dipole model, the magnetic field source is deemed as the magnetic charge. The calculation of the magnetic field intensity follows Magnetic Coulomb's law. Fig. 2 is the schematic of magnetic dipole model. There are two kinds of opposite magnetic charges which evenly distribute along the defect's two sidewalls. The density of magnetic charge

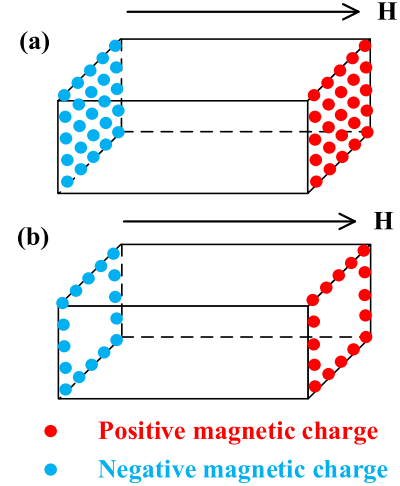


Fig. 3. Distribution of magnetic charges in different magnetization states. (a) Initial magnetization state. (b) Steady magnetization state.

is denoted as ρ_v . And the magnetic field intensity value of an arbitrary point $P(x, y, z)$ can be written as,

$$\mathbf{H} = \mathbf{H}_1 + \mathbf{H}_2 \quad (1)$$

where H_1 and H_2 are the magnetic field intensity of the magnetic charges of the two sidewalls on the arbitrary spatial point $P(x, y, z)$, which can be expressed as following,

$$\mathbf{H}_1 = \int_0^h du \int_{-1}^1 \frac{\rho_v [(x+a)\mathbf{e}_x + (y-u)\mathbf{e}_y + (z-v)\mathbf{e}_z]}{4\pi\mu [(x+a)^2 + (y-u)^2 + (z-v)^2]^{3/2}} dv \quad (2)$$

$$\mathbf{H}_2 = \int_0^h du \int_{-1}^1 \frac{\rho_v [(a-x)\mathbf{e}_x + (u-y)\mathbf{e}_y + (v-z)\mathbf{e}_z]}{4\pi\mu [(a-x)^2 + (u-y)^2 + (v-z)^2]^{3/2}} dv \quad (3)$$

However, in practice, one can find that the magnetic particles mainly distribute along the defect's edges rather than distribute evenly along the defect's sidewalls [17]. Therefore, the principle explanation of the magnetic dipole model need be revised. As illustrated in Fig. 3(a), firstly, the magnetic charges distribute evenly along the cross-section in the initial magnetization state. Then they are diffused by their repulsive force and shift to the defect's edges as shown in Fig. 3(b).

Therefore, the magnetic field intensity value of an arbitrary point $P(x, y, z)$ can be considered as the effect of magnetic charges on ten edges in Fig. 4. Equation (1) can be revised as,

$$\mathbf{H} = \mathbf{H}_{AB} + \mathbf{H}_{BC} + \mathbf{H}_{AD} + \mathbf{H}_{A'B'} + \mathbf{H}_{B'C'} + \mathbf{H}_{A'D'} + \mathbf{H}_{DE} + \mathbf{H}_{ED'} + \mathbf{H}_{CF} + \mathbf{H}_{FC'} \quad (4)$$

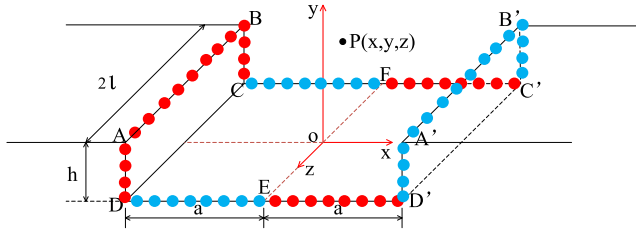


Fig. 4. The revised magnetic dipole model.

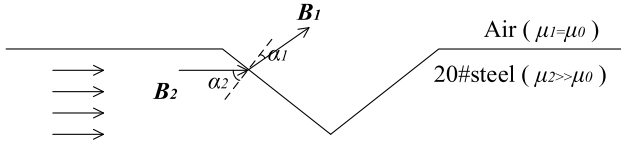


Fig. 5. The schematic of magnetic flux density refraction.

It should be noted that the expression of magnetic field intensity of an arbitrary point $P(x, y, z)$ is complex, and it is too difficult to obtain the specific expression if the defect's shape is irregular.

B. Partial Differential Equations Model

Different from magnetic dipole model, partial differential equations model is based on the hypothesis that magnetic molecular current is the magnetic source. Instead of magnetic field intensity H , magnetic flux density B is used as the elementary parameter to describe the characteristic of magnetic field.

Magnetic flux density discontinuity will occur in two different mediums (20# steel and air for instance) interface as illustrated in Fig. 5.

According to the magnetic field's boundary condition, the angle of magnetic flux density refraction α is related with the permeability μ as shown in (5). We will have $\alpha_1 \ll \alpha_2$ due to $\mu_1 \ll \mu_2$. Hence, the direction of B_1 will be close to the normal direction.

$$\frac{\tan \alpha_1}{\tan \alpha_2} = \frac{\mu_1}{\mu_2} \quad (5)$$

The spatial magnetic flux density can be expressed as following,

$$\mathbf{B} = \nabla \times \mathbf{A} \quad (6)$$

And the magnetic potential A follows the partial difference expression as follows,

$$\begin{cases} \nabla^2 \mathbf{A} = -\mu \mathbf{J}_e + \sigma \mu \left(\frac{\partial \mathbf{A}}{\partial t} + \nabla \varphi \right) \\ \nabla \cdot \left[\sigma \left(\frac{\partial \mathbf{A}}{\partial t} + \nabla \varphi \right) \right] = 0 \end{cases} \quad (7)$$

where \mathbf{J}_e is the excitation current density, σ is the conductivity of 20# steel and φ is the scalar potential of electricity field. The analytical solution of (7) is hard to obtain, but with the help of finite element analysis method (FEM), the numerical solution could be obtained easily as the following shows.

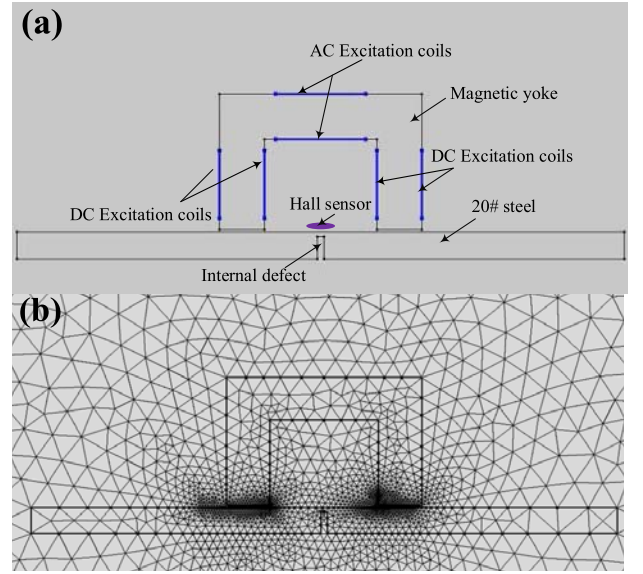


Fig. 6. (a) Schematic diagram of the simulation model. (b) Mesh distribution of the simulation.

TABLE II
PARAMETERS OF SIMULATION MODEL

Parameters	Value
Excitation	AC&DC
Frequency	20-50Hz
DC excitation coil turns	500
DC current intensity	1-1.5A
AC excitation coil turns	500
The amplitude value of AC current	1A
Relative permeability of magnetic yoke	3000
Conductivity of 20# steel	$1 \times 10^6 \text{ S/m}$
Magnetic Characteristic of 20# steel	BH curve
Thickness of 20# steel	12mm
Width of the defect	1-6mm
Lift-off of Hall sensor	1mm

III. FINITE ELEMENT SIMULATION

As shown in Fig. 6(a), a simulation model is built in the COMSOL Multiphysics software. Direct current (DC) and alternating current (AC) are applied in the excitation coils, which are encircled onto the magnetic yoke. A Hall sensor is used to collect the spatial magnetic field signal. Based on Equation (7), a functional is constructed as follows,

$$F(\mathbf{A}) = \iint_D \left(\left(\frac{\partial \mathbf{A}}{\partial x} \right)^2 + \left(\frac{\partial \mathbf{A}}{\partial y} \right)^2 - 2\mu [\mathbf{J}_e - \sigma \left(\frac{\partial \mathbf{A}}{\partial t} + \nabla \varphi \right)] \mathbf{A} \right) dx dy \quad (8)$$

By calculating the extremum of the functional $F(\mathbf{A})$, we can get the solution of Equation (7). The domain of integral D is divided into mesh as shown in Fig. 6(b).

Parameters settings of the simulation model are listed in Table II.

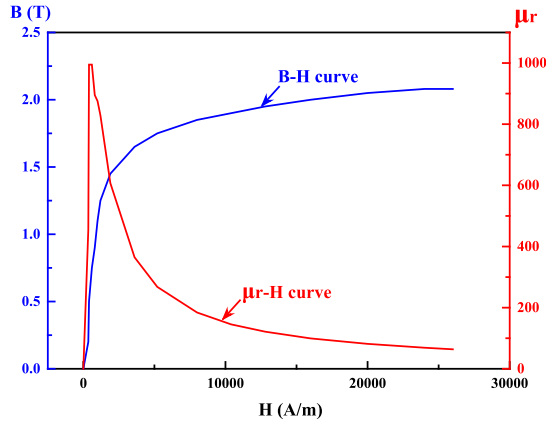


Fig. 7. Magnetic characteristic curves of 20# steel.

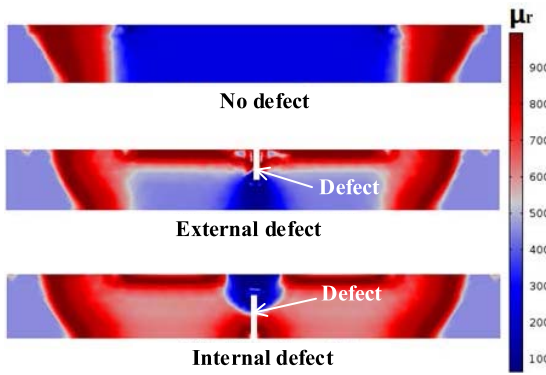


Fig. 8. Permeability distribution of 20# steel plate.

The skin depth δ of the magnetic field in the sample steel (20# steel) has the following expression [4],

$$\delta = \sqrt{1/(\pi \mu f \sigma)} \quad (9)$$

where the μ , f , σ are the permeability, excitation frequency and conductivity respectively.

Under the alternating electromagnetic field, the sample steel (20# steel)'s magnetic flux density changes with the change of the magnetic field intensity according to its B-H curve. Since the relative permeability can be expressed as

$$\mu_r = \mathbf{B}/(\mu_0 \mathbf{H}) \quad (10)$$

we can obtain the $\mu_r - H$ curve as illustrated in Fig. 7. The permeability increases and then decreases gradually with the increase of the magnetic field intensity as shown in Fig. 7.

Consequently, the permeability will be extremely small under a large power excitation. Fig. 8 is the permeability distribution of 20# steel plate. One can see that the high intensity DC excitation makes the 20# steel plate in a saturation state, which will make the permeability value small and increase the value of the skin depth δ . Therefore, if there is a defect in the 20# steel, most of magnetic flux will bypass the defect, which will make the bypassing area in a magnetization saturation state. The permeability in the bypassing area will become smaller and some magnetic flux will leak from the 20# steel as Fig. 9 shows.

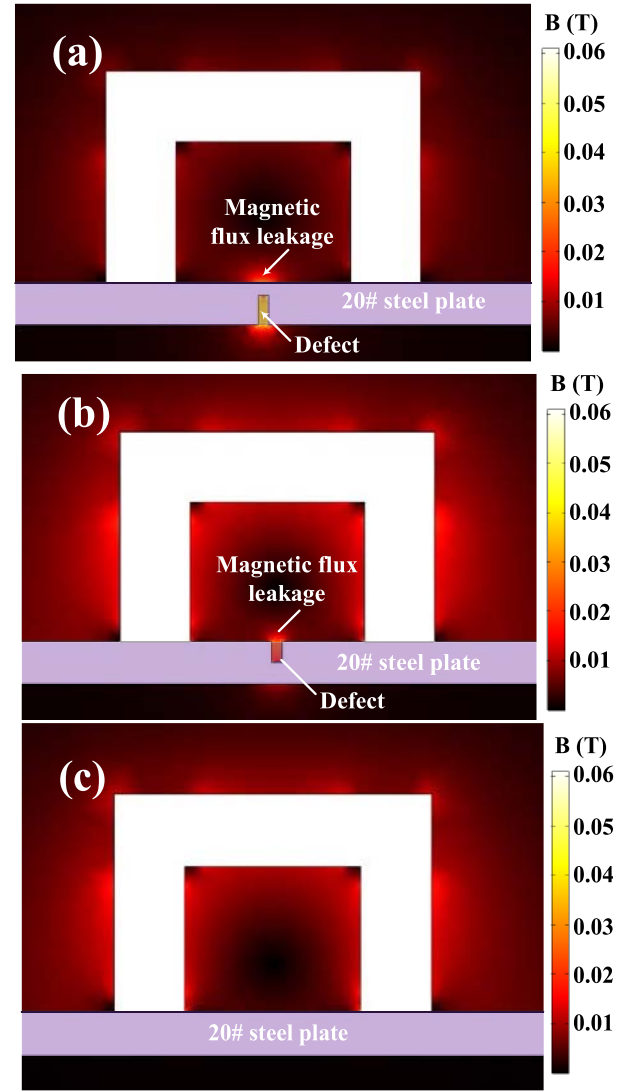


Fig. 9. Distributions of magnetic flux density with (a) internal defect, (b) external defect and (c) no defect in the 20# steel plate.

The simulation results of spatial magnetic field distribution are shown in Fig. 9. Magnetic flux leakage occurs when there is a defect in the 20# steel plate. Hence, by putting the Hall sensor in the leakage area, we can know the existence of the defects.

Fig. 10 shows the simulation results of external defect in 20# steel plate. From Fig. 10, one can see that the absolute of signal trough value increases with the increasing of defect depth.

And there is a remarkable linear relationship between defect depth d and its corresponding signal trough value as shown in Fig. 11. In the depth range of 2 to 8mm, the detection sensitivity is 66.95 Gs/mm.

Fig. 12 shows the detecting results of internal defect. As shown in Fig. 13, with the increasing of buried depth h , the absolute of signal trough value exponentially decreases. Simulation results manifest that an 11mm buried depth of bottom surface defect is detectable in 12mm thickness 20# steel plate.

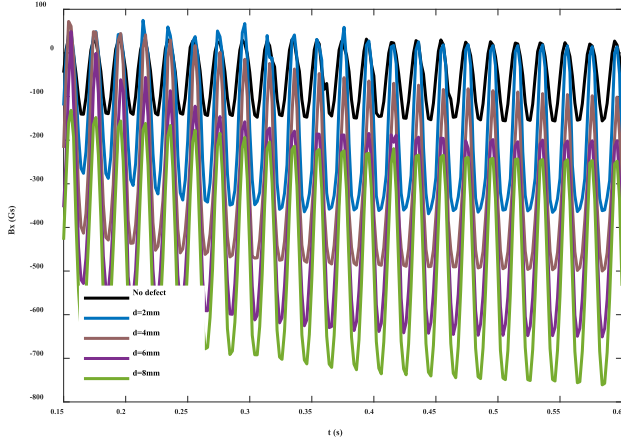


Fig. 10. The magnetic field signals under different external defects' depth d .

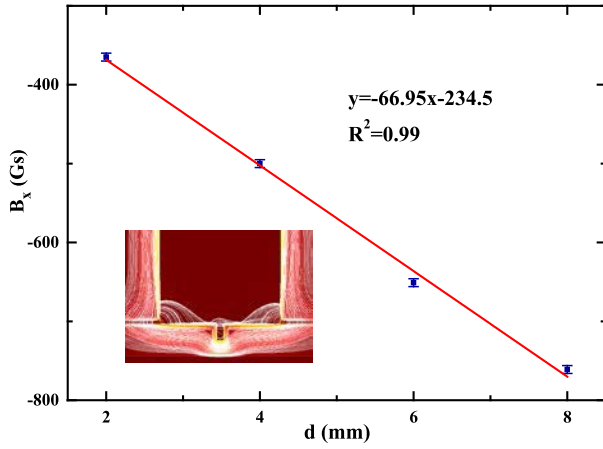


Fig. 11. The relationship between external defect's depth d and amplitude of B_x . Inset: Spatial distribution of the magnetic induction lines.

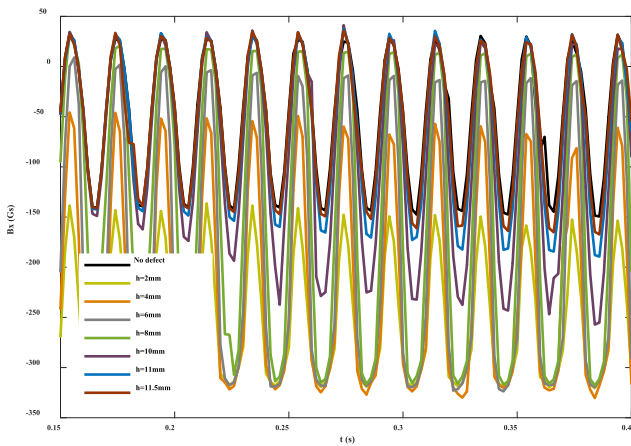


Fig. 12. The magnetic field signals under different internal defects' buried depth h .

IV. EXPERIMENTS

Schematic diagram of the LFET sensor is shown in Fig. 14(a). We use a direct current (DC) source to generate a strong magnetic field to make the steel plate in a magnetic

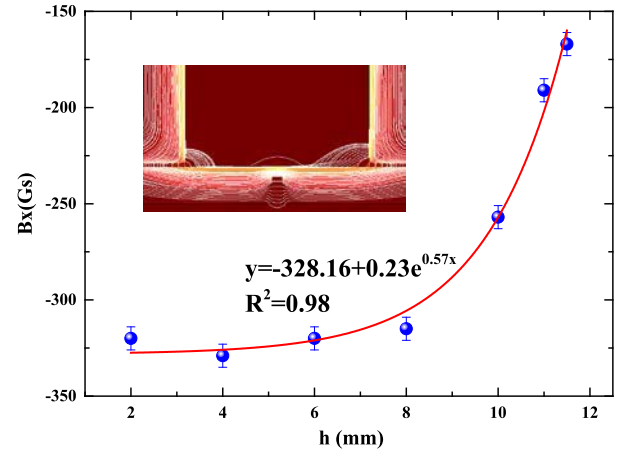


Fig. 13. The relationship between internal defect's buried depth h and amplitude of B_x . Inset: Spatial distribution of the magnetic induction lines.

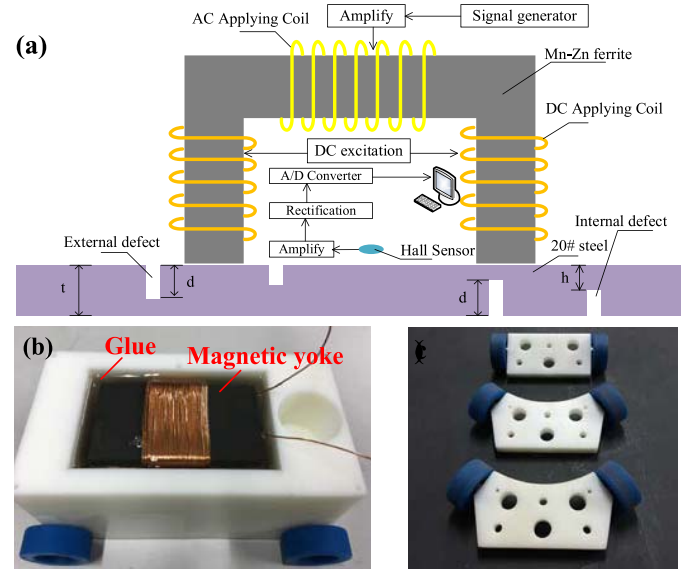


Fig. 14. (a) Schematic diagram of the LFET set-up. (b) Configuration of the LFET sensor. (c) Different curvature axes.

saturation state. Then an alternative current (AC) source is applied. The steel plate's permeability will be smaller, and the skin depth will be deeper when the steel plate is in the magnetic saturation state.

The configuration of the LFET sensor is depicted in Fig. 14(b). A magnetic yoke is immersed in the plotting glue to reduce the signal noise from magnetic yoke's shake. Different curvature axes are made for the detection on different surface curvature pipelines as Fig. 14(c) shows.

Data acquisition card, signal generator, power amplifier and transformer are all put into a multi-function box as Fig. 15 shows. A LabVIEW program is designed to process and show the collected signal.

To verify the validity of the proposed LFET sensor, three internal artificial defects (D1, D2 and D3) are made in a 12 mm-thick 20# steel plate, as shown in Fig. 15. Their parameters are shown in Table III. D1 and D2 are buried blind holes. D3 is a buried rectangular groove.

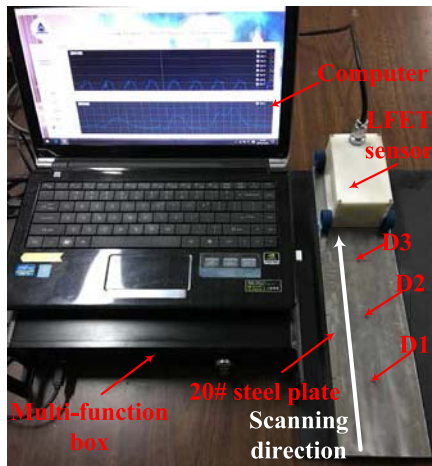


Fig. 15. Illustration of the whole experimental system.

TABLE III
THE PARAMETERS OF THREE ARTIFICIAL DEFECTS

	Diameter (mm)	Buried depth (mm)	Width (mm)
D1	5	6	\
D2	5	5	\
D3	\	6	5

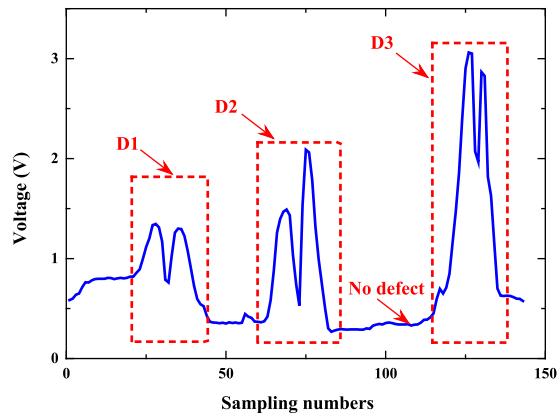


Fig. 16. Scanning signal of internal artificial defects.

The inspection signal is shown in Fig. 16. The scanning velocity is 0.1m/s. And it can be seen that the existence of defects will cause a high peak response compared to the no defect situation.

The experimental scanning signal in Fig. 16 can be explained through Fig. 17 (a) and (b). Fig. 17 (a) is the magnetic induction line of the magnetic flux leakage signal as the defect is located between the two yoke feet. And when the Hall sensor passes five points from P_1 to P_5 , as shown in Fig. 17(b), two peaks responses emerge because the magnetic flux density at P_2 and P_4 is more intensive than other positions. If the width of defect is close to the size of the Hall sensor, one can only get one signal peak. The signal peak value is related to the buried depth of internal defect. The maximum

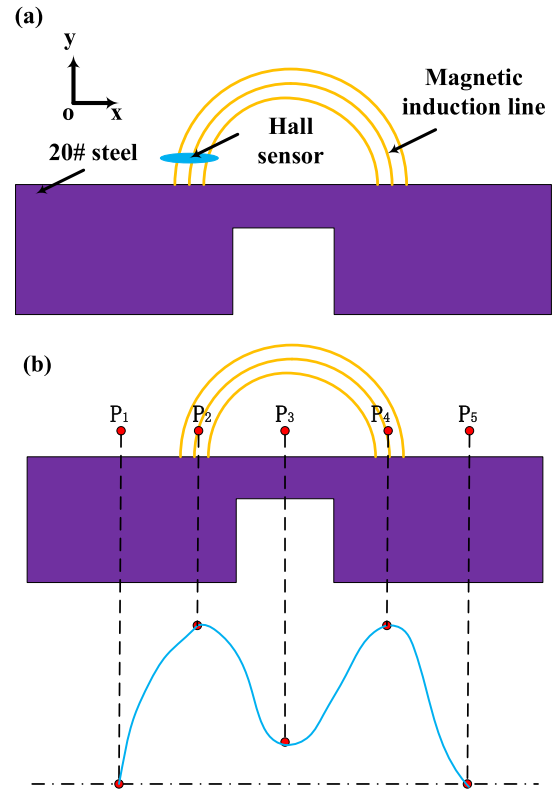


Fig. 17. (a) Magnetic induction line of the magnetic flux leakage signal as the defect is located between the two yoke feet. (b) The signals response of the Hall sensor for different position on the back of the internal defect.

TABLE IV
PARAMETERS AND DETECTING RESULTS OF THE FOUR PIPELINES

The Pipeline number	Wall thickness t(mm)	Nominal diameter (mm)	Buried depth h(mm)	Detecting result(mm)	Relative error
1	6.3	100	5.76	5.71	0.87%
2	7.0	100	5.82	5.89	1.20%
3	6.0	120	5.73	5.78	0.87%
4	6.0	150	5.37	5.46	1.68%

detectable buried depth limitation is the skin depth expressed in Equation (9). In this paper, the skin depth of 20# steel under the parameter settings in TABLE II is 11.25mm ($\mu_r = 100$ can be approximately deemed that magnetization saturation state is attained).

The LFET prototype has also been applied on four kinds of 20# steel pipelines for internal defects detection. Their corresponding parameters and the detecting results are shown in Table IV. The relative error is in a range of 0.87% to 1.68%.

The characteristics comparisons of different detection methods are illustrated in Table V. Compared with other four methods, the LFET sensor proposed in this paper can achieve 50% buried depth detection, which is almost 1.5 times deeper than those depicted in [5], [12], and [17].

TABLE V
CHARACTERISTICS COMPARISONS OF DIFFERENT DETECTION METHODS

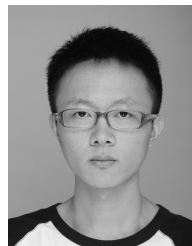
Detection method	Defect location	Material	Defect Width	Detectable Buried depth
SDT sensor [13]	External and internal	Al with ferromagnetic fastener	0.1-4mm	60%
Electromagnetic thermography [12]	External	Stainless steel	1-2mm	\
ECPP thermography [14]	External and internal	Steel 250	1-6mm	40%
TMR-based MFL sensor [5]	External	Carbon steel	0.3-6mm	\
This paper	External and internal	Carbon steel	1-6mm	50%

V. CONCLUSIONS

A LFET sensor based on saturation magnetization method to detect defects in 20# steel was proposed. Compared with conventional MFL technique, the LFET sensor can achieve internal defect detection and 6 mm buried depth can be detected in the 12 mm thickness 20# steel plate. Besides, the proposed LFET sensor can be used for pipe and plate defects detection simultaneously. In the next work, the sensor will be developed and improved for deeper internal defects detection with higher sensitivity.

REFERENCES

- [1] Y. Shi, C. Zhang, R. Li, M. Cai, and G. Jia, "Theory and application of magnetic flux leakage pipeline detection," *Sensors*, vol. 15, no. 12, pp. 31036–31055, 2015.
- [2] Y. Gotoh and N. Takahashi, "Proposal of detecting method of plural cracks and their depth by alternating flux leakage testing: 3-D nonlinear eddy current analysis and experiment," *IEEE Trans. Magn.*, vol. 40, no. 2, pp. 655–658, Mar. 2004.
- [3] Y. Gotoh and N. Takahashi, "Proposal of detecting method of outer side crack by alternating flux leakage testing using 3-D nonlinear FEM," *IEEE Trans. Magn.*, vol. 42, no. 4, pp. 1415–1418, Apr. 2006.
- [4] H. Yamada, T. Hasegawa, Y. Ishihara, T. Kiwa, and K. Tsukada, "Difference in the detection limits of flaws in the depths of multi-layered and continuous aluminum plates using low-frequency eddy current testing," *NDT E Int.*, vol. 41, no. 2, pp. 108–111, 2008.
- [5] B. Wu, Y. J. Wang, X. C. Liu, and C. F. He, "A novel TMR-based MFL sensor for steel wire rope inspection using the orthogonal test method," *Smart Mater. Struct.*, vol. 24, no. 7, p. 075007, 2015.
- [6] B. Han, Q. Xu, and Q. Yuan, "Multiobjective optimization of a combined radial-axial magnetic bearing for magnetically suspended compressor," *IEEE Trans. Ind. Electron.*, vol. 63, no. 4, pp. 2284–2293, Apr. 2016.
- [7] L. Guo, H. Zhang, M. Galea, J. Li, and C. Gerada, "Multiobjective optimization of a magnetically levitated planar motor with multilayer windings," *IEEE Trans. Ind. Electron.*, vol. 63, no. 6, pp. 3522–3532, Jun. 2016.
- [8] J. Chen, S. Huang, and W. Zhao, "Three-dimensional defect reconstruction from magnetic flux leakage signals in pipeline inspection based on a dynamic taboo search procedure," *Insight, Non-Destructive Testing Condition Monit.*, vol. 56, no. 10, pp. 535–540, 2014.
- [9] R. H. Priewald, C. Magele, P. D. Ledger, N. R. Pearson, and J. S. D. Mason, "Fast magnetic flux leakage signal inversion for the reconstruction of arbitrary defect profiles in steel using finite elements," *IEEE Trans. Magn.*, vol. 49, no. 1, pp. 506–516, Jan. 2013.
- [10] K. C. Hari, M. Nabi, and S. V. Kulkarni, "Improved FEM model for defect-shape construction from MFL signal by using genetic algorithm," *IET Sci., Meas., Technol.*, vol. 1, no. 4, pp. 196–200, Jul. 2007.
- [11] Y. Sun, Y. Kang, and C. Qiu, "A permanent magnetic perturbation testing sensor," *Sens. Actuators A, Phys.*, vol. 155, no. 2, pp. 226–232, 2009.
- [12] B. Gao, W. L. Woo, and G. Y. Tian, "Electromagnetic thermography nondestructive evaluation: Physics-based modeling and pattern mining," *Sci. Rep.*, vol. 6, p. 25480, May 2016.
- [13] B. Wincheski, F. Yu, J. Simpon, P. Williams, and K. Rackow, "Development of SDT sensor based eddy current probe for detection of deep fatigue cracks in multi-layer structure," *NDT E Int.*, vol. 43, no. 8, pp. 718–725, 2010.
- [14] Y. He, G. Y. Tian, M. Pan, and D. Chen, "Eddy current pulsed phase thermography and feature extraction," *Appl. Phys. Lett.*, vol. 103, no. 8, p. 084104, 2013.
- [15] S. M. Dutta, F. H. Ghorbel, and R. K. Stanley, "Dipole modeling of magnetic flux leakage," *IEEE Trans. Magn.*, vol. 45, no. 4, pp. 1959–1965, Apr. 2009.
- [16] M. Yan, S. Udpa, S. Mandayam, Y. Sun, P. Sacks, and W. Lord, "Solution of inverse problems in electromagnetic NDE using finite element methods," *IEEE Trans. Magn.*, vol. 34, no. 5, pp. 2924–2927, Sep. 1998.
- [17] W. C. Zhong, "Theoretical fundamentals of magnetic dipole for longitudinal magnetization of a square steel component," *Mater. Eval.*, vol. 57, no. 9, pp. 937–939, 1999.



Weimin Lou was born in Zhejiang, China, in 1993. He received the B.S. degree from the Institute of Optoelectronic Technology, China Jiliang University, Hangzhou, China, in 2015, where he is currently pursuing the master's degree. His main research interests include optical fiber sensor technology and electromagnetic testing technique.



Changyu Shen was born in Hunan, China, in 1977. He received the M.S. degree in optics and optical engineering from Shaanxi Normal University in 2002 and the Ph.D. degree in optics and optical engineering from Zhejiang University in 2009. He is currently a Professor with China Jiliang University. His research interests include tilted fiber Bragg grating sensors, surface plasma resonance fiber optical sensors, hydrogen fiber optical sensors, and electromagnetic testing techniques.

Zhouhong Zhu, photograph and biography not available at the time of publication.

Zexu Liu, photograph and biography not available at the time of publication.

Fengying Shentu, photograph and biography not available at the time of publication.

Weixin Xu, photograph and biography not available at the time of publication.

Tingting Lang, photograph and biography not available at the time of publication.

Yang Zhang, photograph and biography not available at the time of publication.

Zhenguo Jing, photograph and biography not available at the time of publication.

Wei Peng, photograph and biography not available at the time of publication.